

Structure

Higher-Order Architecture of Rhodopsin in Intact Photoreceptors and Its Implication for Phototransduction Kinetics

Highlights

- Molecular resolution of rhodopsin in intact disk membrane
- Four levels of structural organization
- Rhodopsin tracks might kinetically trap preassembled transducin molecules
- Parallel alignment of tracks might be important for polarization sensitivity

Authors

Monika Gunkel,
Johannes Schöneberg, ...,
U. Benjamin Kaupp, Ashraf Al-Amoudi

Correspondence

ashraf.al-amoudi@dzne.de (A.A.-A.),
u.b.kaupp@caesar.de (U.B.K.)

In Brief

Gunkel et al. show by cryo-EM that rhodopsin in intact photoreceptors is hierarchically organized in dimers, rows, and parallel tracks. Simulations suggest that tracks form a kinetic trap for the preassembled G protein transducin.

Higher-Order Architecture of Rhodopsin in Intact Photoreceptors and Its Implication for Phototransduction Kinetics

Monika Gunkel,^{1,4} Johannes Schöneberg,^{3,4} Weaam Alkhalidi,² Stephan Irsen,¹ Frank Noé,³ U. Benjamin Kaupp,^{1,*} and Ashraf Al-Amoudi^{2,*}

¹Department of Molecular Sensory Systems, Center of Advanced European Studies and Research (caesar), Ludwig-Erhard-Allee 2, 53175 Bonn, Germany

²German Center of Neurodegenerative Diseases, Ludwig-Erhard-Allee 2, 53175 Bonn, Germany

³Computational Molecular Biology Group, Freie Universität Berlin, Arnimallee 6, 14195 Berlin, Germany

⁴Co-first author

*Correspondence: ashraf.al-amoudi@dzne.de (A.A.-A.), u.b.kaupp@caesar.de (U.B.K.)

<http://dx.doi.org/10.1016/j.str.2015.01.015>

SUMMARY

The visual pigment rhodopsin belongs to the family of G protein-coupled receptors that can form higher oligomers. It is controversial whether rhodopsin forms oligomers and whether oligomers are functionally relevant. Here, we study rhodopsin organization in cryosections of dark-adapted mouse rod photoreceptors by cryoelectron tomography. We identify four hierarchical levels of organization. Rhodopsin forms dimers; at least ten dimers form a row. Rows form pairs (tracks) that are aligned parallel to the disk incisures. Particle-based simulation shows that the combination of tracks with fast precomplex formation, i.e. rapid association and dissociation between inactive rhodopsin and the G protein transducin, leads to kinetic trapping: rhodopsin first activates transducin from its own track, whereas recruitment of transducin from other tracks proceeds more slowly. The trap mechanism could produce uniform single-photon responses independent of rhodopsin lifetime. In general, tracks might provide a platform that coordinates the spatiotemporal interaction of signaling molecules.

INTRODUCTION

G protein-coupled receptors (GPCRs) mediate cellular responses to hormones and neurotransmitters and they are responsible for the sense of smell, taste, and vision. Some GPCRs form homo- or heterodimers (Audet and Bouvier, 2012; Gurevich and Gurevich, 2008; Lohse, 2010). The most compelling cases for functional heterodimers exist for type C GPCRs (γ -aminobutyric acid B receptors, taste receptors, and metabotropic glutamate receptors). How general this finding is and whether GPCRs besides dimers can form higher-order oligomers is a topic of debate (Gurevich and Gurevich, 2008; Lohse, 2010; Palczewski, 2010). Another debated issue concerns the

functional significance of oligomers, in particular, whether oligomers are required for the activation of G proteins.

A case in point is rhodopsin, the visual pigment in photoreceptors and a founding member of the GPCR family. Rhodopsin is embedded at high density in the membrane of a stack of flattened sacs, called disks. Studies of rhodopsin organization in the disk membrane using various biophysical techniques yielded mixed results. Transient photodichroism and recovery-after-flash-bleaching experiments suggest that rhodopsin is freely diffusing in the disk membrane (Cone, 1972; Liebman and Entine, 1974; Poo and Cone, 1974). However, reappraisal of these experiments revealed a substantial, yet highly variable fraction of immobile rhodopsin (Govardovskii et al., 2009) and heterogeneity of rhodopsin diffusion across the disk membrane (Najafi et al., 2012a). Electron microscopy (EM) and X-ray and neutron diffraction show rhodopsin molecules to be randomly dispersed on the disk (Chabre, 1975; Roof and Heuser, 1982; Saibil et al., 1976), consistent with the notion that rhodopsin is mobile. In two-dimensional (2D) crystals, rhodopsin molecules from frog, bovine, and squid form dimers (Davies et al., 2001; Schertler and Hargrave, 1995; Schertler et al., 1993). Atomic force microscopy (AFM) of isolated disk membranes, adsorbed on a mica surface, revealed randomly oriented rows of rhodopsin dimers and voids that seem to be depleted of rhodopsin molecules (Fotiadis et al., 2003; Jastrzebska et al., 2006). However, another AFM study reported loosely packed rhodopsin molecules in the center of disks, surrounded by a ring of protein-free lipid phase (Buzhynskyy et al., 2011). The different rhodopsin arrangements suggest that interaction between the isolated disk and mica surface alters the distribution of lipid and proteins. Finally, in detergent micelles, rhodopsin can form dimers and higher-order oligomers (Fotiadis et al., 2003; Jastrzebska et al., 2006). However, the functional significance of rhodopsin oligomers is as yet unclear.

Solubilized rhodopsin monomers (Ernst et al., 2007) and monomers in membrane nanodisks (Bayburt et al., 2007; Bulenger et al., 2005; Whorton et al., 2008) can fully activate the G protein transducin (G_t), suggesting that rhodopsin monomers represent the minimal functional unit. Moreover, theoretical studies suggest that, within a reaction-diffusion framework, rhodopsin oligomers do not accelerate the rate of the G_t

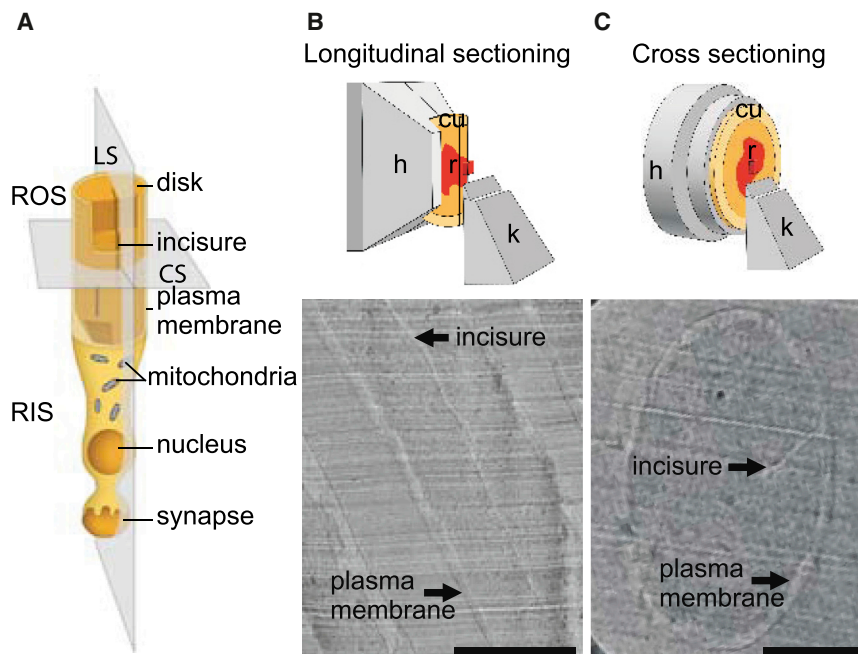


Figure 1. Two-Plane Strategy for Cryosectioning of Intact Retinal Rod Photoreceptors

(A) Schematic overview of cryosectioning of rod photoreceptors. The outer segment (ROS) and inner segment (RIS) are indicated. Gray planes show orientations of cross (CS) and longitudinal (LS) sectioning.

(B) Longitudinal sectioning of a piece of high-pressure frozen retina (r). (Top) Scheme of retina in copper carrier (cu) fixed in a standard ultramicrotome holder (h) for sectioning with a diamond knife (k). (Bottom) Electron micrograph of a longitudinal section. In this view, stacks of disk membranes can be seen.

(C) Cross sectioning of a piece of high-pressure frozen retina. (Top) Copper carrier as in (B) fixed to a specially designed holder to expose the sample from the photoreceptor layer. (Bottom) Electron micrograph of a cross section of a rod photoreceptor. Scale bars, 500 nm.

activation (Dell’Orco and Schmidt, 2008; Schöneberg et al., 2014). However, under physiological conditions, G_t becomes activated at rates well below the diffusion limit (Heck and Hofmann, 2001), suggesting that G_t activation is not optimized for speed and that a supramolecular organization of rhodopsin might serve functions others than kinetics.

Most if not all studies were performed on heterologously expressed GPCRs or under nonnative conditions or were lacking the spatial resolution necessary to resolve single molecules. Here, we study the molecular organization of rhodopsin in intact rod photoreceptors by cryoelectron tomography (cryo-ET). We identify tracks made of rows of rhodopsin dimers that are aligned parallel to the disk incisure. Moreover, using particle-based computer simulation, we examine the functional consequences of the track organization for G_t activation. We find that a track structure in combination with precomplexes between rhodopsin and G_t can lead to biphasic kinetics, thus regulating the phototransduction cascade.

RESULTS

Two-Plane Strategy of Cryosectioning

Small retinal pieces were rapidly cryofixed by high-pressure freezing, which preserves the retina structure under close to native conditions (Al-Amoudi et al., 2007; Hsieh et al., 2006). However, the analysis of cryo-ET tomograms of ultrathin vitreous sections is hampered by (1) deformations (mainly crevasses and compression) that are associated with the cutting direction and (2) the missing wedge due to the restricted angular range of tomographic tilt series. To overcome these limitations, we prepared both longitudinal and cross sections of rod outer segments (ROS) for cryo-EM and tomography (Figure 1). The two-plane sectioning strategy indirectly integrates the information from both views: cross sections provide direct access to the overall organization of the disk surface (top view) with minimal ef-

fect of the missing wedge on the resolution of molecular organization. In longitudinal sections, the structure of disk membranes (side view) is much better preserved and more suitable for high-resolution analysis. Therefore, this strategy provides full access to the native, three-dimensional (3D) arrangement of rhodopsin in the disk membrane. For longitudinal sectioning (plane LS in Figure 1A), the copper carrier containing the frozen retina was fixed in a standard cryosectioning holder (Figure 1B). The longitudinal sections comprised all cell layers throughout the retina thickness, allowing visualization of the entire stack of disk membranes (Figure 1B, bottom, and Movie S1). For cross sectioning (plane CS in Figure 1A), the frozen sample was positioned such that the photoreceptor layer of the retina is facing the knife edge (Figure 1C). The cross sections contained a few disks, allowing a direct view of the disk surface (Figure 1C, bottom, and Movie S2). We acquired hundreds of tomograms of longitudinal and cross sections and from these we reconstructed 3D models of the ROS.

Rhodopsin Is Arranged as Dimers, Rows, and Tracks

A top view of the disk revealed a rough surface with a characteristic texture showing thread-like structures with an average width of 8 nm that evenly occupied the whole disk surface (Figure 2A; Figure S1). A close-up view revealed dumbbell-shaped, electron-dense structures (Figure 2B). We extracted hundreds of subvolumes (called subtomograms) of these threads from across the whole disk surface; thread subtomograms were translationally and rotationally aligned and averaged (Figures S1–S4). Subtomogram averaging considerably enhances the signal-to-noise ratio, thus allowing for quantitative analysis at the molecular level in situ (Al-Amoudi et al., 2007, 2011). To account for potential deformation of the disk surface along the cutting direction during cross sectioning, we tightly masked the extracted subtomograms of the threads with a cylindrical mask to include only one thread with a few dumbbells. An average of extracted regions revealed that threads represent a chain of dumbbell-shaped structures (Figure 2C). We interpret the dumbbells as rhodopsin dimers and the threads as rows of dimers. The

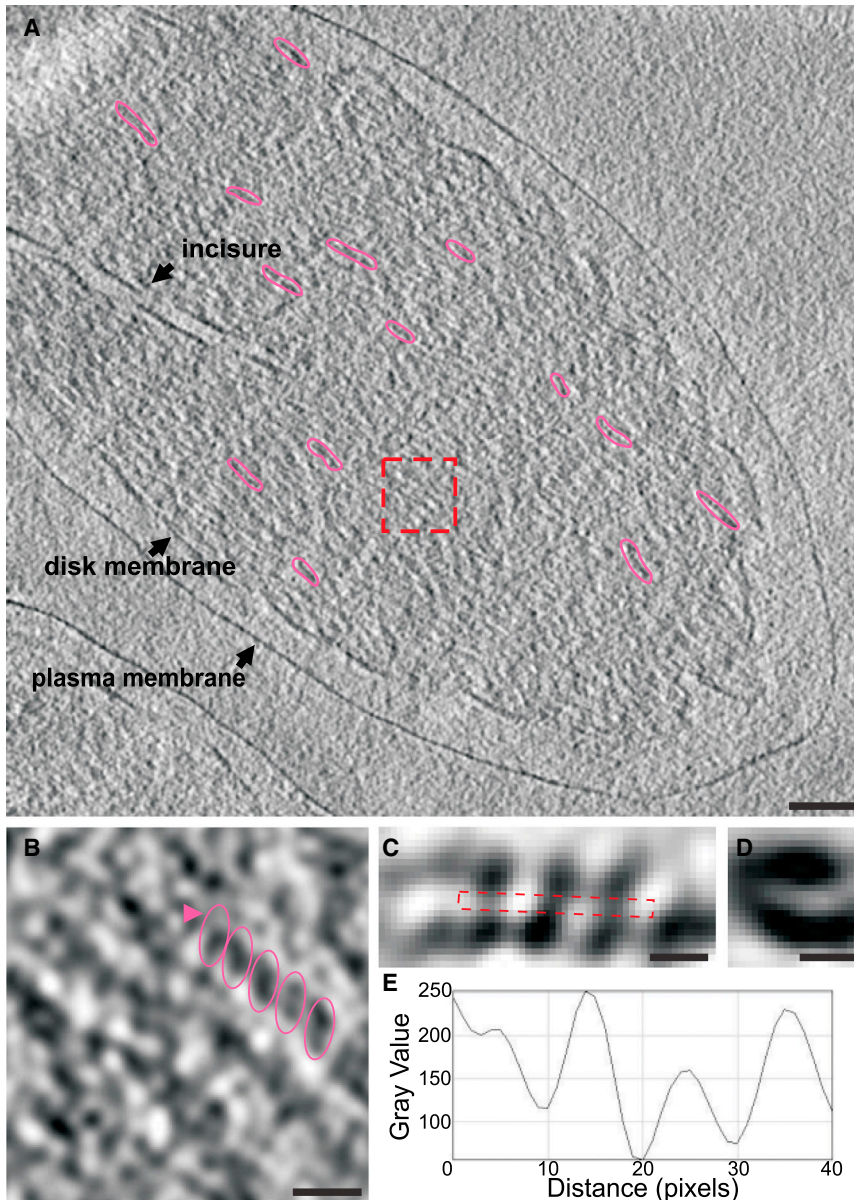


Figure 2. Three-dimensional Analysis of Rhodopsin Arrangement in Cross Sections of Rod Photoreceptors

(A) Tomographic slice through a 3D reconstruction of a cross section of ROS. The disk membrane is densely covered with thread-like structures (examples highlighted by purple contours) oriented approximately parallel to the incisure. Scale bar, 100 nm.

(B) Enlargement of the boxed area in (A) reveals that each thread (purple arrowhead) consists of dumbbell-shaped structures (purple ellipses). The size of the dumbbell is consistent with the size of a rhodopsin dimer. Scale bar, 20 nm.

(C and D) Top and side views of 1,222 translationally and rotationally aligned and averaged subtomograms of threads (see also Figure S1) confirm that the threads represent rows of rhodopsin dimers. Scale bars, 5 nm.

(E) Line profile of the boxed region in (C) showing the repetitive order of dimers within a row with an interdimer distance of ~5 nm. Minima correspond to darker regions. Pixel size, 0.5 nm.

organization: rows are not equidistant, but form pairs that look like railway tracks (double arrows in Figure 3B inset and Figure 3C). The distance between two rows of a track was approximately 5 nm and the distance between two tracks was approximately 15 nm (Table 1).

To gain a more detailed view of the structural organization of a track, we performed subtomogram averaging at full resolution. Approximately 500–1,000 subtomograms were extracted, rotationally and translationally aligned, and averaged (Figure 3; Figure 4). Because of the small size of rhodopsin, we took several measures to resolve single molecules. First, we chose the subtomogram size small enough to permit proper averaging not affected by potential membrane irregularities, but large enough to include one

center-to-center distance of a dimer was approximately 4 nm (Figures 2C and 2D), consistent with the expected size of a dimer (Fotiadis et al., 2003), and the interdimer distance was approximately 5 nm (Figure 2E).

The 3D tomographic reconstruction revealed that rows are aligned almost parallel to the disk incisure (Figure 2A). To minimize potential effects of cutting deformation on higher-order organization of rhodopsin, we analyzed tomograms from longitudinal sections uncompromised by cutting deformations (Figure 3; Figure 4). Analysis of a low-resolution tomogram in a plane parallel to the disk membrane (corresponding to the disk surface), in fact, revealed ordered electron-dense structures of putative rows of rhodopsin dimers running parallel to the incisure (oblique view in Figure 3A and Movie S3). Thus, another structural feature is the precise alignment of rows. Closer inspection of the electron-dense structures revealed a further feature of the rhodopsin

track as the representative unit of the organization. Second, we applied a tight mask corresponding to the size of one disk membrane during the subtomogram alignment. Third, subtomograms were extracted around low intensities corresponding to the positions of rhodopsin in the membrane bilayer (Figure S2). Disk membranes were automatically segmented using mathematical morphological operations (Gonzalez et al., 2009) (Figures S2A and S2B). Because rhodopsin molecules have opposite orientations in the two bilayers of a disk, the disk membranes were classified into even or odd groups and were segmented separately based on an average image of the whole tomogram, taking advantage of the regularity of the disk membrane (Figures S2C and S2D).

Figure 4 shows the structural arrangement of the tracks at full resolution; each track is built from two rows of rhodopsin dimers. The organization of rhodopsin dimers is clearly visible on the

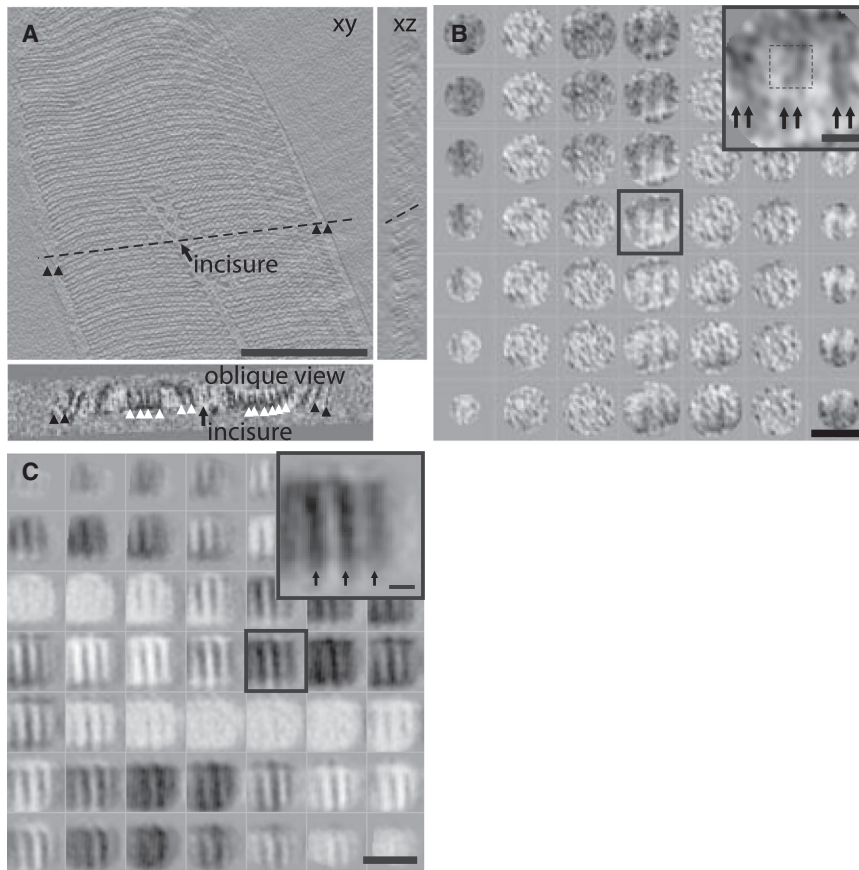


Figure 3. Low-Resolution Analysis of Rhodopsin Arrangement in Longitudinal Sections

(A) Three-view tomographic slices from a longitudinal section. The tomogram has been smoothed by a Gaussian filter and 2x binned in order to enhance the contrast. Three views are shown: xy, xz, and an oblique view. The xy view shows a stack of membranes interrupted at the incisure. Plasma membrane and disk membrane at the rim region are indicated (black arrowheads). The xz view depicts the stack of membranes from the side. The oblique view corresponds to the plane indicated by the dotted lines through one disk membrane in xy and xz views. Electron-dense structures (white arrowheads) running parallel to the incisure can be visualized. Scale bar, 500 nm.

(B) A gallery of a representative subtomogram, seen in a plane corresponding to the oblique view in (A), reveals rail track arrangement of putative rhodopsin molecules. Regions void of tracks correspond to inter- or intradisk space. Scale bar, 80 nm. Inset: double arrows indicate the rail track arrangement. Scale bar, 20 nm.

(C) A gallery of a subtomogram average visualized in a plane parallel to the membrane (top view). The average was computed from the tomogram shown in Figure 3A. The tomogram has been smoothed by a Gaussian filter and 2x binned in order to enhance the contrast. Approximately 160 subtomograms were extracted and rotationally aligned and averaged in order to obtain an initial visual impression on the overall rhodopsin organization in the disk membranes. The average reveals an ordered arrangement of putative rows of rhodopsin dimers. Regions void of structure

correspond to inter- and intradisk spaces. Scale bar, 100 nm. Inset: arrows show the rail track organization of rhodopsin. Because of the big size of the subtomogram volume used here, the structure of the tracks was smoothed out (see Figures 4B and 4C for full-resolution small-sized average track). Scale bar, 20 nm.

inside and top views of the disk membrane with an interdimer distance within a row of approximately 5 nm (Figures 4B and 4C; Table 1). Single rhodopsin molecules can also be clearly visualized (Figures 4B and 4C and Movie S4; see also Figure S4). In the top view, due to the missing-wedge effect, some densities appear elongated along the row axis (Figure 4B); this effect is absent in the side view (Figure 4C). Moreover, tomograms show thin filament-like connections between rows (Figure 4). These connecting filaments (spacer) keep the two rows of a track at a distance of approximately 5 nm. All track dimensions were deduced from several averaged images (Table 1) and are illustrated in a schematic model of the rhodopsin organization on a disk surface (Figure 5A).

Simulation of Transducin Activation Kinetics by Different Rhodopsin Architectures

Particle-based reaction-diffusion simulations were done with the ReaDDy software (Schöneberg and Noe, 2013). The diffusion constant and reaction rates were parametrized as described previously (Schöneberg et al., 2014). To investigate the consequences of a track structure on reaction kinetics, the encounter rate of G_t with rhodopsin and the kinetics of G_t activation were simulated for three different structural scenarios (Figure 5B): (i) rhodopsin and G_t are free to diffuse according to the classic collision-coupling model of signaling by random encounters of mol-

ecules (control); (ii) immobile rhodopsin is organized in tracks; light activates rhodopsin (R^*) either on the outside or inside of a track; and (iii) rhodopsin and G_t form a precomplex RG_t , with a kinetic stability that is determined by on and off rate constants. Although preassembly has yet to be demonstrated *in vivo*, at least simulations and studies using solubilized and reconstituted rhodopsin and G_t suggest preassembly of signaling components (Alves et al., 2005; Dell'Orco and Koch, 2011; Fanelli and Dell'orco, 2008; Kim et al., 2009).

Compared with the control scenario ($\sim 1.4 \times 10^4 \text{ s}^{-1}$; Pugh and Lamb, 1993; Schöneberg et al., 2014), the encounter rate for the track scenario dropped only to about one-half or one-third when R^* is located at the inside or outside of a track, respectively (Figure 6A). The rhodopsin spacing in a track is sufficient to allow for diffusional passage of G_t . The lower rates are largely due to the fact that encounters are controlled only by mobile G_t . The modest drop is functionally irrelevant, because all encounter rates are much larger than the limit set by G_t activation (1000 s^{-1} per R^* ; Figure 6A, dotted line) (Heck and Hofmann, 2001). Thus, an important insight is that the rhodopsin arrangement during diffusional encounter does not rate limit the production of active G_t (G_t^*), and consequently, a track architecture is compatible with physiological kinetics.

Next, we considered an inactive precomplex formed by rhodopsin and G_t and its consequences for G_t activation

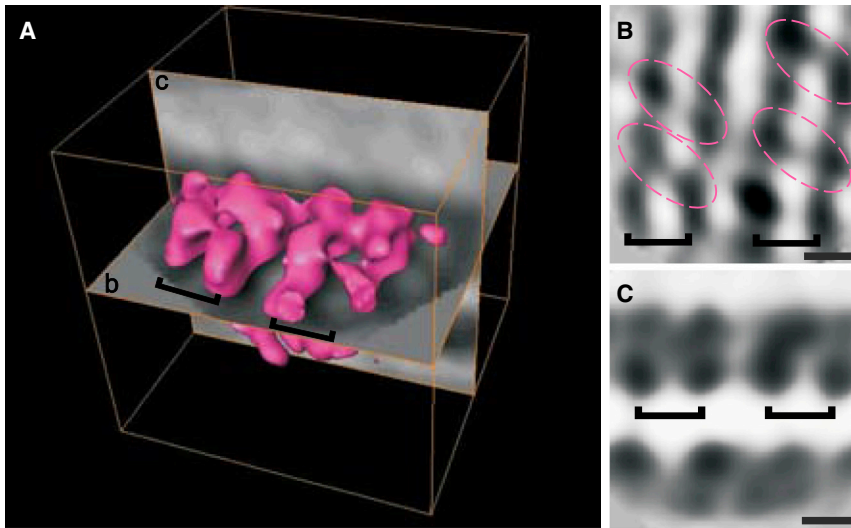


Figure 4. High-Resolution Analysis of Rhodopsin Arrangement in Longitudinal Sections

Subtomogram average of track regions at full resolution. The subtomogram size was chosen such that it includes only one track (corresponding to the dashed box in the inset of Figure 3B). In addition, a tight mask corresponding to the size of one disk membrane was applied during the subtomogram alignment. The average reveals that one track represents double rows of rhodopsin dimers.

(A) Isosurface representation of the subtomogram average (purple).

(B) Slice through the subtomogram average corresponding to the *b* plane in (A). Two parallel rows (black brackets) containing rhodopsin dimers (purple ellipses) can be seen.

(C) Slice through the subtomogram average corresponding to the *c* plane in (A). The rhodopsin dimers (black brackets) as well as individual monomers are clearly visible (see also Figures S4E and S4F). Note that the upper membrane was used for the average; the lower one has been masked out. Scale bars, 5 nm.

(Figure 5B, scenario iii). It is known that precomplex formation reduces the encounter rate between G_t and R^* (Schöneberg et al., 2014). For the track architecture, the precomplex dissociation rate must be $\geq 3 \times 10^4 \text{ s}^{-1}$ to achieve the speed limit of G_t activation; otherwise, diffusional encounters become rate-limiting (Figure 6B). Here, for the first time, we investigate the combined effect of rhodopsin architecture and inactive RG_t precomplexes on G_t^* production via formation and subsequent decay of an active R^*G_t complex (Figure 6C). When no inactive precomplexes are formed, the G_t^* production increases linearly with time, independent of the R architecture (free or in tracks). For these two scenarios, a large variance in the R^* lifetime would directly result in a large variance in the G_t^* output (see also Schöneberg et al., 2014). In contrast, for strong but short-lived precomplexes and for a large range of kinetic parameters (Figure S5 and Movie S5), rhodopsin tracks serve as kinetic traps for preassociated G_t . This behavior gives rise to biphasic kinetics: diffusion and activation of precomplexed G_t within a track are much faster than the exchange of G_t molecules between tracks. Such a mechanism gives rise to a robust G_t^* response that is largely independent of the R^* lifetime (Figure 6C).

DISCUSSION

In summary, by integrating information from tomograms of cross and longitudinal sections, we identify, for the first time, the highly ordered arrangement of rhodopsin molecules in the disk membrane of intact photoreceptors with molecular resolution. Due to the small size of rhodopsin (40 kDa), the resulting molecular map was not amenable to fitting with the X-ray structure of rhodopsin. However, the resolution was sufficient to identify monomers and dimers. Our data provide compelling evidence of rhodopsin dimers, as building blocks of a hierarchical supra-molecular architecture. Our results confirm previous studies using AFM on isolated mica-supported disks (Fotiadis et al., 2003). However, our study on intact photoreceptors adds two new features. The structure is characterized by aligned rows of dimers

and pairs of rows (tracks). Tracks and their parallel alignment might subserve several functions.

Molecule Preassembly on Tracks Does Not Slow Down Activation Kinetics

Rhodopsin tracks might represent functional modules that direct the spatiotemporal and stoichiometric interaction of preassembled signaling molecules. Our simulations illustrate that the organization of immobile rhodopsin does not prevent G_t^* activation from being efficient: no matter where in a track rhodopsin is activated, G_t^* production is not rate limited by diffusional encounter of R^* and G_t . Moreover, preassembly does not affect G_t^* production either, provided the formation and dissociation rates are sufficiently fast. For high binding constants, i.e. when most G_t molecules are precomplexed, the dissociation rate of the precomplex must be $\geq 3 \times 10^4 \text{ s}^{-1}$. Otherwise, G_t proteins are stuck with rhodopsin and activation kinetics is slowed down.

Preassembly of G_t has been studied in vitro using solubilized rhodopsin and G_t molecules (Alves et al., 2005; Dell'Orco and Koch, 2011; Fanelli and Dell'orco, 2008; Kim et al., 2009). However, high-affinity sites for preassembly might involve several rhodopsin molecules in a track and might require G_t tethered to the disk membrane via its isoprenyl modification. For example, G_t could be accommodated in the groove between the two rows of a track. Our study underscores the need to study preassembly of signaling molecules in intact photoreceptors.

Tracks as Kinetic Traps

Precomplex formation in combination with a track arrangement results in a remarkable behavior: for a large parameter range of precomplex formation (Figure S5), the tracks kinetically trap G_t molecules. Owing to the frequent, rapid formation and breakup of precomplexes, G_t proteins could scan a track by discrete hopping events (Dell'Orco and Koch, 2011). When G_t meets an active R^* , an $R^*G_t^*$ complex is formed, which eventually decays to R^* and G_t^* with a rate of about 1000 s^{-1} (see Movie S5). Consequently, a single R^* first activates all preassembled G_t in

Table 1. Structure Parameters of Rhodopsin and Disks

Parameter	Value
Distance between monomers in a dimer	4.3 ± 0.4 nm
Distance between dimers in a row	5.5 ± 0.4 nm
Distance between two rows in a rail track	5.7 ± 0.3 nm
Distance between two tracks	15 ± 3 nm
Length of a row	At least 10 dimers (~50 nm)
Rhodopsin density	~20,000 molecules μm^{-2}
Interdisk space	16 ± 1.6 nm (14 ± 3 nm) ^a
Intradisk space	4.6 ± 1.4 nm (4 ± 1 nm) ^a
Disk thickness	19 ± 2 nm (21 ± 1 nm) ^a
Disk membrane thickness	7.0 ± 1.3 nm (8 ± 1 nm) ^a

The table shows the mean distances ± SD. Distances were measured from four data sets. A total of approximately 100 positions were measured to compute the mean distances. The dimensions of the oligomeric track structure of rhodopsin were deduced from averaged data.

^aThe disk dimensions are similar to those from Nickell et al. (2007), in which plunge freezing was performed. Thus, the cutting-induced deformations have no significant effect on the disk structure.

a track. About 50–100 ms after R* activation, the G_t* production slows down, because additional G_t molecules must be recruited from neighboring tracks.

This mechanism predicts that, in the single-photon regime, the G_t* production is determined by the number of the preassembled G_t molecules per track rather than the R* lifetime. Consistent with this mechanism, the mean single-photon response is little dependent on the expression level of rhodopsin kinase that initiates R* inactivation, but rather on the expression level of a regulator of G protein signaling (RGS) that controls the lifetime of G_t* (Krispel et al., 2006). Provided that the number of G_t molecules per track is about constant, this trap mechanism could produce uniform single-photon responses and, thereby, reduce photon noise. Other mechanisms previously proposed that could accomplish similar consequences are reproducible rhodopsin deactivation (Mendez et al., 2000; Doan et al., 2006), spatiotemporal filtering by diffusion of cyclic guanosine monophosphate (Bisegna et al., 2008; Caruso et al., 2010), and Ca²⁺ feedback (Gross et al., 2012).

For an R/G_t ratio of 10:1 (Pugh and Lamb, 2000), a minimal track of about 50 nm in length is built from about 40 rhodopsin molecules and maximally four preassembled G_t molecules. Considering a mean R* lifetime of 36 ms and a G_t activation rate of 240 s⁻¹, as few as eight G_t molecules are activated by a single R* (Burns and Pugh, 2010; Cangiano and Dell'Orco, 2013; Gross and Burns, 2010); thus, the number of G_t activated per R* is of the same order as the number of preassembled G_t molecules per unit track. However, this estimate is fraught with uncertainties. A lower physical limit for the track length is set by the thickness of longitudinal sections (about 50 nm). Moreover, crevasses formed during cryosectioning might have disrupted longer tracks. Therefore, rhodopsin tracks might be longer and accommodate more G_t molecules than this lower limit. Finally, the track length might not be uniform.

Rhodopsin Might Serve a Structural Role

Rhodopsin tracks could shape and maintain the overall structure of disks and ROS. Although, rhodopsin monomers interact

directly to form dimers, cytoskeletal filaments might pattern rows and tracks on the disk surface. Previous EM studies reveal thin filaments between disks (about one spacer per 50 rhodopsin molecules) (Nickell et al., 2007; Roof and Heuser, 1982) and axial filaments along incisures (Eckmiller, 2000), which might underlie the orientation of rhodopsin rows. Thus, the incisure represents a center of rhodopsin organization. AFM images of fragmented disks are lacking incisures and the orderly alignment of rows is missing (Fotiadis et al., 2003; Jastrzebska et al., 2006). During sample preparation for AFM, filaments involved in the track organization might be severed. The rearrangement of rows could also lead to an overestimate of rhodopsin density (30,000–55,000 molecules μm^{-2} (Fotiadis et al., 2003), twice the density of 20,000 molecules μm^{-2} determined from EM tomograms (Table 1).

A change in the expression level of rhodopsin alters the morphology of ROS and disks (Makino et al., 2012; Wen et al., 2009). Moreover, rhodopsin mutations result in gross changes in ROS morphology and eventually retinal degeneration (Hollingsworth and Gross, 2012), suggesting that rhodopsin is involved in the formation and maintenance of disks. A failure to properly align rhodopsin rows could underlie these devastating diseases. Unlike mammalian photoreceptors, which usually possess only one incisure, disks of amphibian photoreceptors possess up to 20 incisures (Najafi et al., 2012a). It will be interesting to study how rhodopsin rows are oriented in photoreceptors with multiple incisures.

Tracks as Buffering Sites for Signaling Molecules

Light exposure stimulates a massive redistribution of key signaling proteins, like G_t, between the inner and outer segments of rods (Calvert et al., 2006) a process that contributes to photoreceptor adaptation. The mechanism of protein translocation (driven by passive diffusion or molecular motors) is debated (Calvert et al., 2006). We propose that rhodopsin tracks provide a structural platform to buffer signaling components on the disk; thereby, in the dark, signaling components are concentrated in the outer segment. Light stimulation might disrupt either the rhodopsin tracks altogether or the buffering sites on the tracks. Consequently, precomplexed G_t and other components might be released and thus be free to diffuse into the inner segment. Such a mechanism would also favor the idea of redistribution by diffusion rather than active transport (Calvert et al., 2006; Najafi et al., 2012b).

Polarization Sensitivity and Rhodopsin Mobility

The precise alignment of rhodopsin immobilized in tracks could provide the structural basis for polarization sensitivity. A prerequisite of polarization sensitivity of animal vision is the ability to analyze the electrical field vector of incident light with highly orientated chromophores of visual pigments. The polarization sensitivity of many insects is well established; it relies on the precise alignment of rhodopsin in microvilli of photoreceptors (Horvath and Varju, 2004). In contrast, for ciliary photoreceptors of the vertebrate eye, polarization sensitivity is not well established. Moreover, the underlying mechanisms are not clear (Horvath and Varju, 2004; Roberts et al., 2011), not least because the rotational and translational mobility of rhodopsin (Cone, 1972; Liebman and Entine, 1974) would prevent chromophores being aligned along a preferred direction. Rhodopsin mobility has

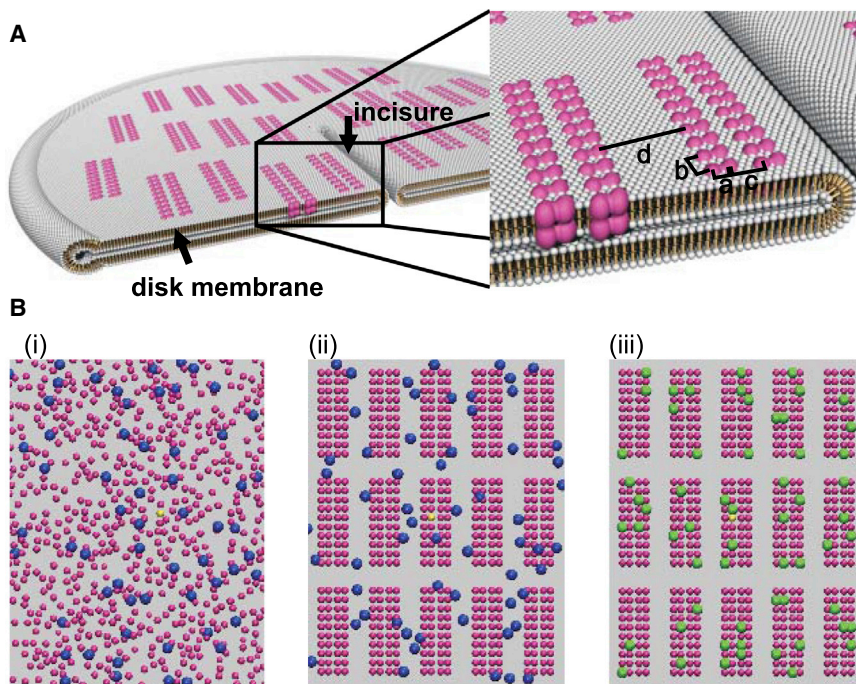


Figure 5. Model of Rhodopsin Organization in the Disk Membrane

(A) The model shows an overview of the organization of rhodopsin (purple) in the intact disk membrane. Four levels of organization are shown: dimerization of rhodopsin monomers with a center-to-center distance of 4 nm (a); dimers form rows with a dimer-to-dimer distance of 5 nm (b); rows come in pairs separated by 5 nm (c); two pairs of rows (tracks) are separated by 15 nm (d) (see also Table 1).

(B) Simulation setups for membrane patches with physiological protein number densities of R, G_q (blue) and a single active R* (yellow) in a freely diffusing system (i), in a track geometry without precomplexes (ii), and in a track geometry in which R and G_q form a precomplex (green, iii).

Cryosectioning of Vitrified Retina

Frozen samples were transferred to the cryochamber of a Leica EM FC6/UC6 or FC7/UC7 ultramicrotome (Leica Microsystems) for cryosectioning. Retina sample blocks were prepared using a 20° trimming diamond knife and cryosectioned at -160°C with a nominal section thickness of 40–50 nm, using a 35° sectioning diamond knife at a cutting speed of 1.0 mm s⁻¹ (Al-Amoudi et al.,

2007). To obtain full access to the rhodopsin arrangement in rod photoreceptors, the frozen retina was sectioned in two orientations, parallel and perpendicular to the ROS axis, hereafter termed longitudinal and cross sections, respectively (Figure 1). Using this two-plane strategy, we indirectly integrate the information from both views by overcoming the effects of the missing wedge usually associated with electron tomography and by minimizing the effect of the cutting-induced deformation along the cutting direction such as crevasses and compression. Cutting deformations usually have no significant effect at molecular resolution (Al-Amoudi et al., 2007; Pierson et al., 2011). The bilayer of disk membranes is well preserved (see Figure S2). For cross cryosectioning, we designed a special holder in which the frozen sample was fixed, such that photoreceptors of the retina are facing the knife edge (Figure 1B). The holder is made of a spring-loaded metal in order to accommodate the sample carrier without too much pressure, which induces cracks inside frozen samples. Sections were collected on copper grids covered with holy carbon film (Quantifoil, 200 mesh, Electron Microscopy Sciences) and attached using the charging system provided with the microtome (CRION, Leica Microsystems). Some cryosections, while attached to the grid, were labeled with quantum dots by dipping the grids for a few seconds in a solution containing 5.3 nmol ml⁻¹ quantum dots in toluene (NIR PbS Core EviDots, Evident Technologies) and diluted in isopentane (Merck) to a concentration of 2% (v/v) according to the protocol of Masich et al. (2006). Sample grids were stored in liquid nitrogen until imaging.

EXPERIMENTAL PROCEDURES

Cryopreservation of Mouse Retina

Mice (C57Bl/6J), Janvier, approximately 8 weeks old) were sacrificed with isoflurane (1-chloro-2,2,2-trifluoroethyl-difluoromethyl ether, Abbott) and additional neck fracture. Because of the high sensitivity of rhodopsin (absorption of a single photon can activate the visual cascade), eyes were removed under dim-red light to avoid photobleaching. Eyes were removed and placed in PBS containing (in mM): 137 NaCl, 2.7 KCl, 10 Na₂HPO₄, 2 KH₂PO₄; pH 7.4 was adjusted with NaOH. The eyeball was opened by cutting around the lens and the vitreous body was removed. The retina was gently separated from the pigment epithelium and pieces of approximately 1 mm² were cut with a scalpel and transferred to a droplet of cryoprotectant containing 20% dextran (Dextran 40, M, 40 kDa; Roth) and 5% sucrose. Four to six pieces were obtained from one retina. The pieces were kept for 5 min in the cryoprotectant. Similar protocols of cryoprotection were previously used for different types of tissues such as retina, brain, and skin (Al-Amoudi et al., 2007, 2011; Wilson et al., 1998; Zuber et al., 2005). The retina slices were electrophysiologically and morphologically well preserved (Wilson et al., 1998). Retina pieces were placed rod photoreceptors facing up into 3 mm copper carriers (0.15 mm indentation, Engineering Office M. Wohlwend). The carrier was filled with the cryoprotectant and closed with a cover that was dipped into chloroform 0.5% phosphatidylcholine (L- α -phosphatidylcholine type XVI-E, Sigma Aldrich) to facilitate opening the sandwich after freezing (Cohen et al., 2008). The specimen was immediately inserted into the high-pressure freezer (HPM100, Leica Microsystems) and frozen in liquid nitrogen pressurized at 2,100 bar.

2007). To obtain full access to the rhodopsin arrangement in rod photoreceptors, the frozen retina was sectioned in two orientations, parallel and perpendicular to the ROS axis, hereafter termed longitudinal and cross sections, respectively (Figure 1). Using this two-plane strategy, we indirectly integrate the information from both views by overcoming the effects of the missing wedge usually associated with electron tomography and by minimizing the effect of the cutting-induced deformation along the cutting direction such as crevasses and compression. Cutting deformations usually have no significant effect at molecular resolution (Al-Amoudi et al., 2007; Pierson et al., 2011). The bilayer of disk membranes is well preserved (see Figure S2). For cross cryosectioning, we designed a special holder in which the frozen sample was fixed, such that photoreceptors of the retina are facing the knife edge (Figure 1B). The holder is made of a spring-loaded metal in order to accommodate the sample carrier without too much pressure, which induces cracks inside frozen samples. Sections were collected on copper grids covered with holy carbon film (Quantifoil, 200 mesh, Electron Microscopy Sciences) and attached using the charging system provided with the microtome (CRION, Leica Microsystems). Some cryosections, while attached to the grid, were labeled with quantum dots by dipping the grids for a few seconds in a solution containing 5.3 nmol ml⁻¹ quantum dots in toluene (NIR PbS Core EviDots, Evident Technologies) and diluted in isopentane (Merck) to a concentration of 2% (v/v) according to the protocol of Masich et al. (2006). Sample grids were stored in liquid nitrogen until imaging.

Cryoelectron Microscopy and Tomography

Sections were imaged with a Titan Krios (FEI Company) operating at 300 kV in the low-dose mode. The state of vitreous water in the cryosections was verified by electron diffraction. Vitreous sections with good morphology were selected for tomographic data collection. Tomograms were recorded on a 4k × 4k Falcon Direct Electron Detector (FEI Company) at magnifications of 14,000x, 22,500x, and 29,000x corresponding to pixel sizes of 0.5, 0.3, and 0.25 nm at the specimen level, with a defocus of -3 or -6 μ m. Samples were tilted from -65° to +65° with tilt increments of 1° or 1.5°. The total dose of each tomogram was adjusted to less than 60 e⁻ Å⁻². Tomographic tilt series acquisition was performed using the Xplore3D software (FEI Company).

Alignment and 3D Reconstruction of Tomograms

Tomograms without quantum dots were aligned with respect to a common origin using cross-correlation techniques (Castano-Diez et al., 2010) and

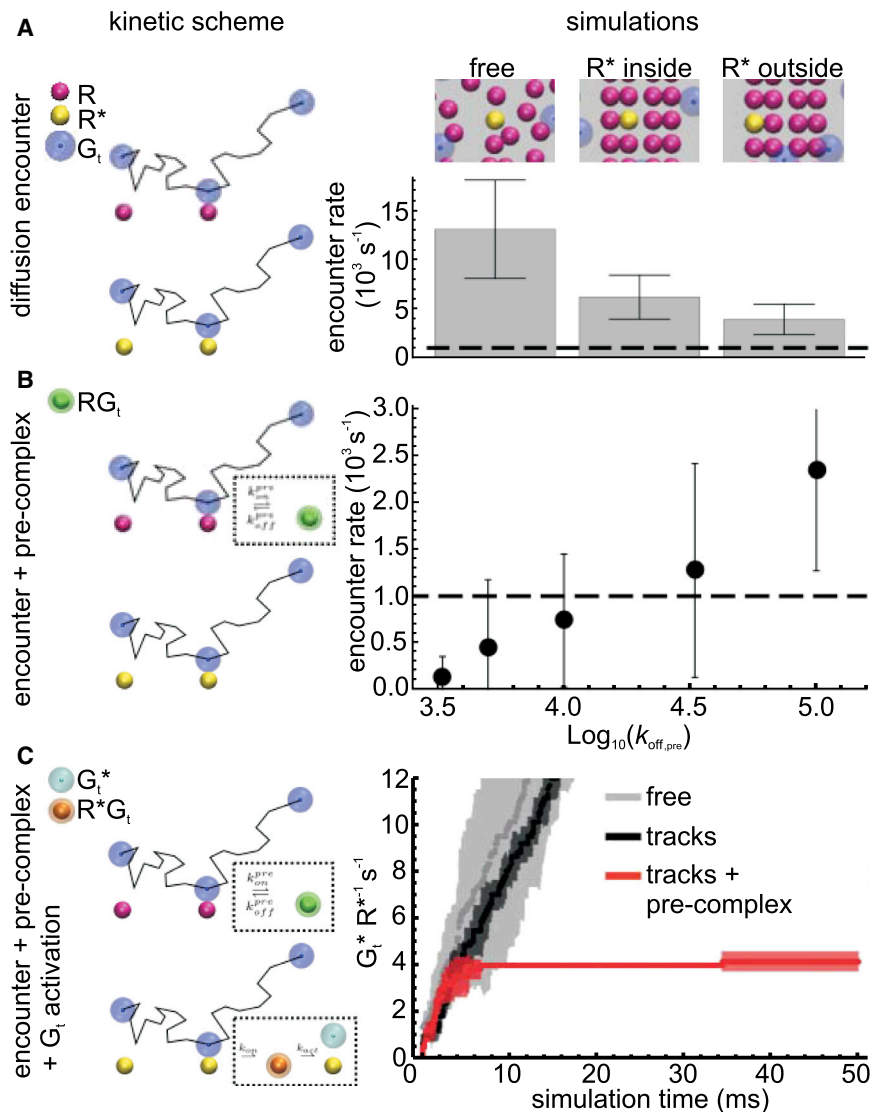


Figure 6. Track Geometry Modulates Activation Kinetics and Gives Rise to Kinetic Partitioning. Particle-based Simulations Probe Protein Diffusion and G_t Activation on the Disk in Three Scenarios:

(A) Diffusional encounters of G_t (blue) with either R (purple) or R^* (yellow) are counted for scenarios when all molecules are freely diffusing (free), and when R is arranged in tracks, with R^* on the inside or on the outside. In neither case does the G_t - R^* encounter rate become rate limiting compared with the G_t activation speed limit of 1000 s^{-1} (Heck and Hofmann, 2001) (dashed line).

(B) Model in which R and G_t engage in an inactive precomplex (RG_t , green); $k_{\text{off,pre}}$ must be $\geq 3 \times 10^4 \text{ s}^{-1}$ such that RG_t dissociation is not rate limiting for G_t^* production.

(C) Model for the full activation kinetics including active (R^*G_t , orange) complexes that decay to R^* and G_t^* (light blue). In the absence of inactive RG_t precomplexes, G_t^* production is linear in time (gray and black activation curves). For appropriate kinetic parameters of precomplex formation (see Figure S5 for details), rhodopsin tracks act as kinetic traps for G_t , giving rise to biphasic kinetics (red activation curve).

ical operations (Gonzalez et al., 2009). Because rhodopsin molecules have opposite orientations in the two bilayers of a disk, we developed an algorithm to classify them into even or odd groups and segmented them separately based on an average image of the whole tomogram, taking advantage of the regularity of the disk membranes (Figure S2). This procedure ensures that only subtomograms with intact membranes are extracted for subsequent subtomogram averaging.

Subtomogram Averaging and Classification of Disk Membranes

To investigate the possible oligomeric arrangement of rhodopsin within the disk membrane, we first analyzed the data at low resolution by filtering

etomo (Mastronarde, 1997), whereas tomograms with quantum dots were aligned with etomo. Using several quantum dots as fiducial markers, we chose tomograms with alignment errors of less than 0.5 nm, indicating well-attached and rigid cryosections. This was particularly possible with the aid of quantum dots, which also helped during the recording of the tilt series. Poorly focused tilt series often resulted in an alignment error larger than 1 nm and, thus, were discarded. The reconstructions were generated using weighted back-projection algorithms, and isosurface visualization was performed by the Amira software package (Mercury Computer Systems) (Movies S1, S2, and S3).

Segmentation of Disks

To perform 3D averaging (see below for the procedure), we first segmented the disk region in both cross as well as longitudinal sections. The 3D reconstructions were denoised with nonlinear anisotropic diffusion (Frangakis and Hegerl, 2001) or Gaussian filters. For cross sections, the 3D tomogram was first segmented using multiple thresholds-based techniques (Otsu, 1979). The regions (rows) of interest are expected to span the class of the lowest intensity level. The pixels of the corresponding class are then isolated and further processed using a combination of mathematical morphological operations (Gonzalez et al., 2009) in order to keep the putative rows of rhodopsin (Figure S2). The segmented rows were used for subtomograms averaging (see below for the procedure of subtomogram averaging). For longitudinal sections, disk membranes were automatically segmented using mathematical morpholog-

and binning the 3D reconstructions in order to enhance the contrast. A 3D low-resolution subtomogram average is shown in Figure 3C. Highly organized structures can be identified. Putative rhodopsin forms pairs of rows resembling rail tracks, and the regions between membranes appear unstructured at this resolution (see also Figure 3B). At this stage, we cannot identify the oligomeric arrangement of rhodopsin (see below for high-resolution analysis).

For the subtomogram averaging, we performed the following procedure: at the skeletonized regions of disk membranes (see e.g. Figure S2), we selected pixels with low intensity values and extracted subtomograms around these positions. For high-resolution analysis, the subtomogram size was selected to include one rail track corresponding to one paired row of rhodopsin dimers as the representative unit of the rhodopsin organization in the disk membrane. This corresponds to approximately 20–24 nm. This subtomogram size produced the best results, considering the flexibility of disk membranes, and was sufficient to resolve the oligomeric arrangement of rhodopsin. For the starting reference, we either selected representative subtomograms or created a reference from those subtomograms that have been extracted. Due to the highly ordered structure of rhodopsin in our tomograms, both procedures worked equally well. Here, we did not use a template or external reference in order to avoid biasing. We aligned the subtomograms rotationally, assuming that the translational shifts of subtomograms were approximately correct. Initially, we determined two out of the three Euler angles (psi and theta corresponding to rotation around the z and x axes) using Radon or Hough

transformation (Figure S3) (Al-Amoudi et al., 2007). The third angle (i.e. the phi angle) was searched during the alignment procedure. We performed the alignment and averaging iteratively using the av3 toolbox (Förster and Hegerl, 2007) or PEET (Cope et al., 2011); both programs gave similar results. For averaging with PEET, we followed a procedure implemented in the software: one rotation axis was defined as a vector between two detected points along the bilayer of the disk membrane. The other two axes of rotation were defined orthogonal to the first one. This was particularly useful for averaging the disk membrane, considering the fine irregularity of the membranes. Because of the highly ordered organization of rhodopsin observed in our tomograms, the angular search was limited to a small range for all the angles. Scanning larger ranges converged to similar results. We observed few subtomograms that contain no clear structures, typically those with deformed membranes. In order to keep only acceptable subtomograms, we classified subtomograms with multivariate statistical analysis using the av3 toolbox (Förster and Hegerl, 2007; Förster et al., 2008). Similar to the averaging, the missing wedge was taken into account in the classification. Representative classes are shown in Figures S4A–S4D. After refinement, high-resolution subtomogram averaging was generated (Figures S4E and S4F). The resolution was estimated by the 0.5 criterion of the Fourier shell correlation to be $(3.4 \text{ nm})^{-1}$.

Particle-Based Reaction-Diffusion Simulations

To investigate the kinetics of G_t activation by R^* , particle-based reaction-diffusion simulations were performed for different scenarios with the ReaDDy software package version 1.1 (Schöneberg and Noe, 2013), similar to Schöneberg et al. (2014). The model simulates the diffusion of particles (such as G_t) using Brownian dynamics (Ermak and McCammon, 1978) through a given topology (such as tracks of rhodopsin). Reactions between a pair of educt particles that form a product particle were determined by their reaction radii (r_r). ReaDDy is able to model reaction-diffusion dynamics for specific cellular architectures and molecular arrangements, even when molecule species are not well mixed. In contrast to other programs of particle-based reaction kinetics (Erban and Chapman, 2009 and references therein), ReaDDy also considers interaction potentials between particles, similar to molecular dynamics simulations. Simulations used purely repulsive interaction potentials that prevented particle overlap. All particle species are resolved explicitly as single particles with collision and reaction radii r_c and r_r , respectively; particles undergo Brownian motion with a microscopic diffusion constant (D_{micro}). Parametrization of particle radii is performed based on crystal structures as in Schöneberg et al. (2014). D_{micro} is set such that the macroscopic diffusion constant (D) adopts known values ($0.7 \mu\text{m}^2 \text{s}^{-1}$ for R and $1.2 \mu\text{m}^2 \text{s}^{-1}$ for G_t) (Pugh and Lamb, 1993) in a free diffusion scenario at 295 K (Schöneberg and Noe, 2013).

There are three types of particle parametrizations in the model: R-type, G_t -type, and RG_t -type. They consist of membrane integral collision radii ($r_{c,\text{integral}}$), radii that govern the collision of parts that float on top of the membrane ($r_{c,\text{float}}$), reaction radii (r_r) and microscopic diffusion constants (D_{micro}). The R-type comprises the active (R^*) and inactive form of rhodopsin (R) which are modeled with $r_{c,\text{integral}} = 2.1 \text{ nm}$, $r_{c,\text{float}} = 0$, $r_r = 2.1 \text{ nm}$ (Salom et al., 2006), and $D_{\text{micro}} = 1.4 \mu\text{m}^2 \text{s}^{-1}$. The G_t -type comprises active (G_t^*) and inactive forms of G_t , modeled with radii $r_{c,\text{integral}} = 0.6 \text{ nm}$, $r_{c,\text{float}} = 3.4 \text{ nm}$, $r_r = 3 \text{ nm}$ (Lambright et al., 1996), and $D_{\text{micro}} = 2.0 \mu\text{m}^2 \text{s}^{-1}$. Particles of RG_t -type comprise RG_t (pre-complex) and R^*G_t (activation complex) with $r_{c,\text{integral}} = 2.1 \text{ nm}$, $r_{c,\text{float}} = 3.4 \text{ nm}$, and $D_{\text{micro}} = 1.4 \mu\text{m}^2 \text{s}^{-1}$. For the RG_t complex, no bimolecular reactions are included in the model, rendering a reaction radius not applicable. Particles undergo 2D diffusion on a membrane patch of $157 \text{ nm} \times 200 \text{ nm}$, giving rise to 600 copies of R, from which one is activated, and 60 copies of G_t . R is distributed either uniformly or in 15 tracks each built from 40 R, exactly resembling the topological parameters derived from subtomogram averaging (Table 1). Particle repulsion and 2D diffusion on a plane are achieved via harmonic softcore potentials with force constants of $10 \text{ kJ mol}^{-1} \text{ nm}^{-2}$. Time is discretized in steps of 10 ns. Our simulation setup resembles other 2D models of the primary photoactivation cascade that consider individual particle copies (Dell'Orco and Schmidt, 2008; Felber et al., 1996; Lamb, 1996) but resolves space continuously, thus permitting the modeling of detailed spatial arrangements such as rhodopsin tracks with their precise measurements.

To investigate the diffusion-limited rate of G_t^* production, the diffusional encounters of R^* with G_t were counted, assuming an instantaneous conversion of G_t into G_t^* upon hitting R^* (Figure 6A). To test the influence of precomplexes, a

precomplex reaction was added to the system (Figure 6B). The diffusional encounter of R and G_t led to the formation of RG_t with rate $k_{\text{on,pre}}$; RG_t dissociates with rate $k_{\text{off,pre}}$.

G_t activation rates have been measured to be in the order of maximally 1000 s^{-1} per R^* (Heck and Hofmann, 2001). Therefore, G_t activation (Figure 6; Movie S5) is modeled as a two-step process. When R^* and G_t meet, an activation complex is formed, which then decays to R^* and G_t^* with rate $k_{\text{act}} = 1000 \text{ s}^{-1}$.

SUPPLEMENTAL INFORMATION

Supplemental Information includes five figures and five movies and can be found with this article online at <http://dx.doi.org/10.1016/j.str.2015.01.015>.

AUTHOR CONTRIBUTIONS

M.G., A.A., and U.B.K. conceived the project and experiments. M.G., A.A., and S.I. designed and executed EM experiments. J.S. and F.N. designed and analyzed simulations experiments. A.A. and W.A. analyzed data. M.G., A.A., and U.B.K. wrote the manuscript. All authors read and corrected the manuscript.

ACKNOWLEDGMENTS

We thank H. Krause for preparing the manuscript, Dr. Bernsdorff and Dr. Pascal for preparing figures and Dr. Ishikawa, Dr. Wallace and Dr. Frangakis for careful reading of and comments on an earlier version of the manuscript.

Received: December 10, 2014

Revised: January 16, 2015

Accepted: January 22, 2015

Published: February 26, 2015

REFERENCES

- Al-Amoudi, A., Diez, D.C., Betts, M.J., and Frangakis, A.S. (2007). The molecular architecture of cadherins in native epidermal desmosomes. *Nature* *450*, 832–838.
- Al-Amoudi, A., Castano-Diez, D., Devos, D.P., Russell, R.B., Johnson, G.T., and Frangakis, A.S. (2011). The three-dimensional molecular structure of the desmosomal plaque. *Proc. Natl. Acad. Sci. USA* *108*, 6480–6485.
- Alves, I.D., Salgado, G.F., Salamon, Z., Brown, M.F., Tollin, G., and Hruby, V.J. (2005). Phosphatidylethanolamine enhances rhodopsin photoactivation and transducin binding in a solid supported lipid bilayer as determined using plasmon-waveguide resonance spectroscopy. *Biophys. J.* *88*, 198–210.
- Audet, M., and Bouvier, M. (2012). Restructuring g-protein-coupled receptor activation. *Cell* *151*, 14–23.
- Bayburt, T.H., Leitz, A.J., Xie, G., Oprian, D.D., and Sligar, S.G. (2007). Transducin activation by nanoscale lipid bilayers containing one and two rhodopsins. *J. Biol. Chem.* *282*, 14875–14881.
- Bisegna, P., Caruso, G., Andreucci, D., Shen, L., Gurevich, V.V., Hamm, H.E., and DiBenedetto, E. (2008). Diffusion of the second messengers in the cytoplasm acts as a variability suppressor of the single photon response in vertebrate phototransduction. *Biophys. J.* *94*, 3363–3383.
- Bulenger, S., Marullo, S., and Bouvier, M. (2005). Emerging role of homo- and heterodimerization in G-protein-coupled receptor biosynthesis and maturation. *Trends Pharmacol. Sci.* *26*, 131–137.
- Burns, M.E., and Pugh, E.N., Jr. (2010). Lessons from photoreceptors: turning off g-protein signaling in living cells. *Physiology (Bethesda)* *25*, 72–84.
- Buzhynskyy, N., Salesse, C., and Scheuring, S. (2011). Rhodopsin is spatially heterogeneously distributed in rod outer segment disk membranes. *J. Mol. Recogn.* *24*, 483–489.
- Calvert, P.D., Strissel, K.J., Schiesser, W.E., Pugh, E.N., Jr., and Arshavsky, V.Y. (2006). Light-driven translocation of signaling proteins in vertebrate photoreceptors. *Trends Cell Biol.* *16*, 560–568.
- Cangiano, L., and Dell'Orco, D. (2013). Detecting single photons: a supramolecular matter? *FEBS Lett.* *587*, 1–4.

- Caruso, G., Bisegna, P., Lenoci, L., Andreucci, D., Gurevich, V.V., Hamm, H.E., and DiBenedetto, E. (2010). Kinetics of rhodopsin deactivation and its role in regulating recovery and reproducibility of rod photoresponse. *PLoS Comput. Biol.* 6, e1001031.
- Castano-Diez, D., Scheffer, M., Al-Amoudi, A., and Frangakis, A.S. (2010). Alignator: a GPU powered software package for robust fiducial-less alignment of cryo tilt-series. *J. Struct. Biol.* 170, 117–126.
- Chabre, M. (1975). X-ray diffraction studies of retinal rods. I. Structure of the disc membrane, effect of illumination. *Biochim. Biophys. Acta* 382, 322–335.
- Cohen, M., Santarella, R., Wiesel, N., Mattaj, I., and Gruenbaum, Y. (2008). Electron microscopy of lamin and the nuclear lamina in *Caenorhabditis elegans*. *Methods Cell Biol.* 88, 411–429.
- Cone, R.A. (1972). Rotational diffusion of rhodopsin in the visual receptor membrane. *Nat. New Biol.* 236, 39–43.
- Cope, J., Heumann, J., and Hoenger, A. (2011). Cryo-electron tomography for structural characterization of macromolecular complexes. *Curr. Protoc. Protein Sci. Chapter 17*, Unit17.13.
- Davies, A., Gowen, B.E., Krebs, A.M., Schertler, G.F., and Saibil, H.R. (2001). Three-dimensional structure of an invertebrate rhodopsin and basis for ordered alignment in the photoreceptor membrane. *J. Mol. Biol.* 314, 455–463.
- Dell’Orco, D., and Koch, K.W. (2011). A dynamic scaffolding mechanism for rhodopsin and transducin interaction in vertebrate vision. *Biochem. J.* 440, 263–271.
- Dell’Orco, D., and Schmidt, H. (2008). Mesoscopic Monte Carlo simulations of stochastic encounters between photoactivated rhodopsin and transducin in disc membranes. *J. Phys. Chem. B* 112, 4419–4426.
- Doan, T., Mendez, A., Detwiler, P.B., Chen, J., and Rieke, F. (2006). Multiple phosphorylation sites confer reproducibility of the rod’s single-photon responses. *Science* 313, 530–533.
- Eckmiller, M.S. (2000). Microtubules in a rod-specific cytoskeleton associated with outer segment incisures. *Vis. Neurosci.* 17, 711–722.
- Erban, R., and Chapman, S.J. (2009). Stochastic modelling of reaction-diffusion processes: algorithms for bimolecular reactions. *Phys. Biol.* 6, 046001.
- Ermak, D.L., and McCammon, J.A. (1978). Brownian dynamics with hydrodynamic interactions. *J. Chem. Phys.* 69, 1352.
- Ernst, O.P., Gramse, V., Kolbe, M., Hofmann, K.P., and Heck, M. (2007). Monomeric G protein-coupled receptor rhodopsin in solution activates its G protein transducin at the diffusion limit. *Proc. Natl. Acad. Sci. USA* 104, 10859–10864.
- Fanelli, F., and Dell’orco, D. (2008). Dark and photoactivated rhodopsin share common binding modes to transducin. *FEBS Lett.* 582, 991–996.
- Felber, S., Breuer, H.P., Petruccione, F., Honerkamp, J., and Hofmann, K.P. (1996). Stochastic simulation of the transducin GTPase cycle. *Biophys. J.* 71, 3051–3063.
- Förster, F., and Hegerl, R. (2007). Structure determination in situ by averaging of tomograms. In *Methods in Cell Biology: Cellular Electron Microscopy*, Vol. 79, J.R. McIntosh, ed. (Academic Press), pp. 741–767.
- Förster, F., Pruggnaller, S., Seybert, A., and Frangakis, A.S. (2008). Classification of cryo-electron sub-tomograms using constrained correlation. *J. Struct. Biol.* 161, 276–286.
- Fotiadis, D., Liang, Y., Filipek, S., Saperstein, D.A., Engel, A., and Palczewski, K. (2003). Atomic-force microscopy: rhodopsin dimers in native disc membranes. *Nature* 421, 127–128.
- Frangakis, A.S., and Hegerl, R. (2001). Noise reduction in electron tomographic reconstructions using nonlinear anisotropic diffusion. *J. Struct. Biol.* 135, 239–250.
- Gonzalez, R.C., Woods, R.E., and Eddins, S.L. (2009). *Digital Image Processing Using MATLAB*, Second Edition. (Gatesmark Publishing).
- Govardovskii, V.I., Korenyak, D.A., Shukolyukov, S.A., and Zueva, L.V. (2009). Lateral diffusion of rhodopsin in photoreceptor membrane: a reappraisal. *Mol. Vis.* 15, 1717–1729.
- Gross, O.P., and Burns, M.E. (2010). Control of rhodopsin’s active lifetime by arrestin-1 expression in mammalian rods. *J. Neurosci.* 30, 3450–3457.
- Gross, O.P., Pugh, E.N., Jr., and Burns, M.E. (2012). Calcium feedback to cGMP synthesis strongly attenuates single-photon responses driven by long rhodopsin lifetimes. *Neuron* 76, 370–382.
- Gurevich, V.V., and Gurevich, E.V. (2008). How and why do GPCRs dimerize? *Trends Pharmacol. Sci.* 29, 234–240.
- Heck, M., and Hofmann, K.P. (2001). Maximal rate and nucleotide dependence of rhodopsin-catalyzed transducin activation: initial rate analysis based on a double displacement mechanism. *J. Biol. Chem.* 276, 10000–10009.
- Hollingsworth, T.J., and Gross, A.K. (2012). Defective trafficking of rhodopsin and its role in retinal degenerations. *Int. Rev. Cell Mol. Biol.* 293, 1–44.
- Horvath, G., and Varju, D. (2004). *Polarized Light in Animal Vision*. (Springer).
- Hsieh, C.E., Leith, A., Mannella, C.A., Frank, J., and Marko, M. (2006). Towards high-resolution three-dimensional imaging of native mammalian tissue: electron tomography of frozen-hydrated rat liver sections. *J. Struct. Biol.* 153, 1–13.
- Jastrzebska, B., Fotiadis, D., Jang, G.F., Stenkamp, R.E., Engel, A., and Palczewski, K. (2006). Functional and structural characterization of rhodopsin oligomers. *J. Biol. Chem.* 281, 11917–11922.
- Kim, T.Y., Uji-i, H., Moller, M., Muis, B., Hofkens, J., and Alexiev, U. (2009). Monitoring the interaction of a single G-protein key binding site with rhodopsin disk membranes upon light activation. *Biochemistry* 48, 3801–3803.
- Krispel, C.M., Chen, D., Melling, N., Chen, Y.J., Martemyanov, K.A., Quillinan, N., Arshavsky, V.Y., Wensel, T.G., Chen, C.K., and Burns, M.E. (2006). RGS expression rate-limits recovery of rod photoresponses. *Neuron* 51, 409–416.
- Lamb, T.D. (1996). Gain and kinetics of activation in the G-protein cascade of phototransduction. *Proc. Natl. Acad. Sci. USA* 93, 566–570.
- Lambright, D.G., Sondek, J., Bohm, A., Skiba, N.P., Hamm, H.E., and Sigler, P.B. (1996). The 2.0 Å crystal structure of a heterotrimeric G protein. *Nature* 379, 311–319.
- Liebman, P.A., and Entine, G. (1974). Lateral diffusion of visual pigment in photoreceptor disk membranes. *Science* 185, 457–459.
- Lohse, M.J. (2010). Dimerization in GPCR mobility and signaling. *Curr. Opin. Pharmacol.* 10, 53–58.
- Makino, C.L., Wen, X.H., Michaud, N.A., Covington, H.I., DiBenedetto, E., Hamm, H.E., Lem, J., and Caruso, G. (2012). Rhodopsin expression level affects rod outer segment morphology and photoresponse kinetics. *PLoS One* 7, e37832.
- Masich, S., Ostberg, T., Norlen, L., Shupliakov, O., and Daneholt, B. (2006). A procedure to deposit fiducial markers on vitreous cryo-sections for cellular tomography. *J. Struct. Biol.* 156, 461–468.
- Mastrorade, D.N. (1997). Dual-axis tomography: an approach with alignment methods that preserve resolution. *J. Struct. Biol.* 120, 343–352.
- Mendez, A., Burns, M.E., Roca, A., Lem, J., Wu, L.W., Simon, M.I., Baylor, D.A., and Chen, J. (2000). Rapid and reproducible deactivation of rhodopsin requires multiple phosphorylation sites. *Neuron* 28, 153–164.
- Najafi, M., Haeri, M., Knox, B.E., Schiesser, W.E., and Calvert, P.D. (2012a). Impact of signaling microcompartment geometry on GPCR dynamics in live retinal photoreceptors. *J. Gen. Physiol.* 140, 249–266.
- Najafi, M., Maza, N.A., and Calvert, P.D. (2012b). Steric volume exclusion sets soluble protein concentrations in photoreceptor sensory cilia. *Proc. Natl. Acad. Sci. USA* 109, 203–208.
- Nickell, S., Park, P.S., Baumeister, W., and Palczewski, K. (2007). Three-dimensional architecture of murine rod outer segments determined by cryo-electron tomography. *J. Cell Biol.* 177, 917–925.
- Otsu, N. (1979). Threshold selection method from gray-level histograms. *IEEE T. Syst. Man. Cyb.* 9, 62–66.
- Palczewski, K. (2010). Oligomeric forms of G protein-coupled receptors (GPCRs). *Trends Biochem. Sci.* 35, 595–600.
- Pierson, J., Ziese, U., Sani, M., and Peters, P.J. (2011). Exploring vitreous cryo-section-induced compression at the macromolecular level using electron cryo-tomography; 80S yeast ribosomes appear unaffected. *J. Struct. Biol.* 173, 345–349.

- Poo, M.-M., and Cone, R.A. (1974). Lateral diffusion of rhodopsin in the photoreceptor membrane. *Nature* 247, 438–441.
- Pugh, E.N., Jr., and Lamb, T.D. (1993). Amplification and kinetics of the activation steps in phototransduction. *Biochim. Biophys. Acta* 1141, 111–149.
- Pugh, E.N.J., and Lamb, T.D. (2000). Phototransduction in vertebrate rods and cones: molecular mechanisms of amplification, recovery and light adaptation. In *Handbook of Biological Physics*, D.G. Stavenga, W.J. DeGrip, and E.N.J. Pugh, eds. (Elsevier Science), pp. 183–255.
- Roberts, N.W., and Needham, M.G. (2007). A mechanism of polarized light sensitivity in cone photoreceptors of the goldfish *Carassius auratus*. *Biophys. J.* 93, 3241–3248.
- Roberts, N.W., Porter, M.L., and Cronin, T.W. (2011). The molecular basis of mechanisms underlying polarization vision. *Philos. Trans. R. Soc. Lond. B Biol. Sci.* 366, 627–637.
- Roof, D.J., and Heuser, J.E. (1982). Surfaces of rod photoreceptor disk membranes: integral membrane components. *J. Cell Biol.* 95, 487–500.
- Saibil, H., Chabre, M., and Worcester, D. (1976). Neutron-diffraction studies of retinal rod outer segment membranes. *Nature* 262, 266–270.
- Salom, D., Lodowski, D.T., Stenkamp, R.E., Le Trong, I., Golczak, M., Jastrzebska, B., Harris, T., Ballesteros, J.A., and Palczewski, K. (2006). Crystal structure of a photoactivated deprotonated intermediate of rhodopsin. *Proc. Natl. Acad. Sci. USA* 103, 16123–16128.
- Schertler, G.F., and Hargrave, P.A. (1995). Projection structure of frog rhodopsin in two crystal forms. *Proc. Natl. Acad. Sci. USA* 92, 11578–11582.
- Schertler, G.F.X., Villa, C., and Henderson, R. (1993). Projection structure of rhodopsin. *Nature* 362, 770–772.
- Schöneberg, J., and Noe, F. (2013). ReaDDy—a software for particle-based reaction-diffusion dynamics in crowded cellular environments. *PLoS One* 8, e74261.
- Schöneberg, J., Heck, M., Hofmann, K.P., and Noe, F. (2014). Explicit spatio-temporal simulation of receptor-G protein coupling in rod cell disk membranes. *Biophys. J.* 107, 1042–1053.
- Wen, X.H., Shen, L., Brush, R.S., Michaud, N., Al-Ubaidi, M.R., Gurevich, V.V., Hamm, H.E., Lem, J., Dibenedetto, E., Anderson, R.E., et al. (2009). Overexpression of rhodopsin alters the structure and photoresponse of rod photoreceptors. *Biophys. J.* 96, 939–950.
- Whorton, M.R., Jastrzebska, B., Park, P.S., Fotiadis, D., Engel, A., Palczewski, K., and Sunahara, R.K. (2008). Efficient coupling of transducin to monomeric rhodopsin in a phospholipid bilayer. *J. Biol. Chem.* 283, 4387–4394.
- Wilson, M.T., Farmer, M.A., and Karwoski, C.J. (1998). Ultrastructure of the frog retina after high-pressure freezing and freeze substitution. *J. Microsc.* 189, 219–235.
- Zuber, B., Nikonenko, I., Klauser, P., Muller, D., and Dubochet, J. (2005). The mammalian central nervous synaptic cleft contains a high density of periodically organized complexes. *Proc. Natl. Acad. Sci. USA* 102, 19192–19197.

Structure, Volume 23

Supplemental Information

**Higher-Order Architecture of Rhodopsin in
Intact Photoreceptors and Its Implication for
Phototransduction Kinetics**

**Monika Gunkel, Johannes Schöneberg, Weaam Alkhaldi, Stephan Irsen, Frank Noé,
U. Benjamin Kaupp, and Ashraf Al-Amoudi**

Supplemental Figures

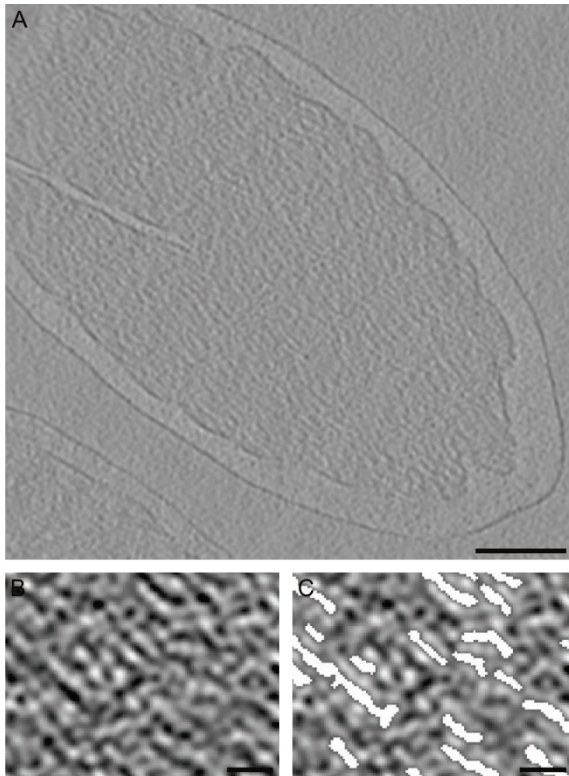


Figure S1, related to Figure 2. Segmentation of Disk Region of a Cross Section

(A) 3D reconstruction of a cross section showing individual putative rows of rhodopsin dimers in the disk surface. The reconstruction was denoised and 2x binned in order to enhance the visualization of the rows for the illustration of the procedure thus individual rhodopsin molecules are not visible. For high-resolution analysis, full-resolution data were used (Figures 2C-2E). (Scale bar 200 nm).

(B) Cropped region from part (A).

(C) Overlay of the same region in (B) with the corresponding extracted segments in white. The image was first segmented using multiple thresholds-based techniques (Otsu, 1979). The regions (rows) of interest are expected to be spanning the class of low intensity level. The pixels of the corresponding class are then isolated and further processed using a combination

of mathematical morphological operations in order to keep the rows. (Scale bars in (B) and (C) 40 nm).

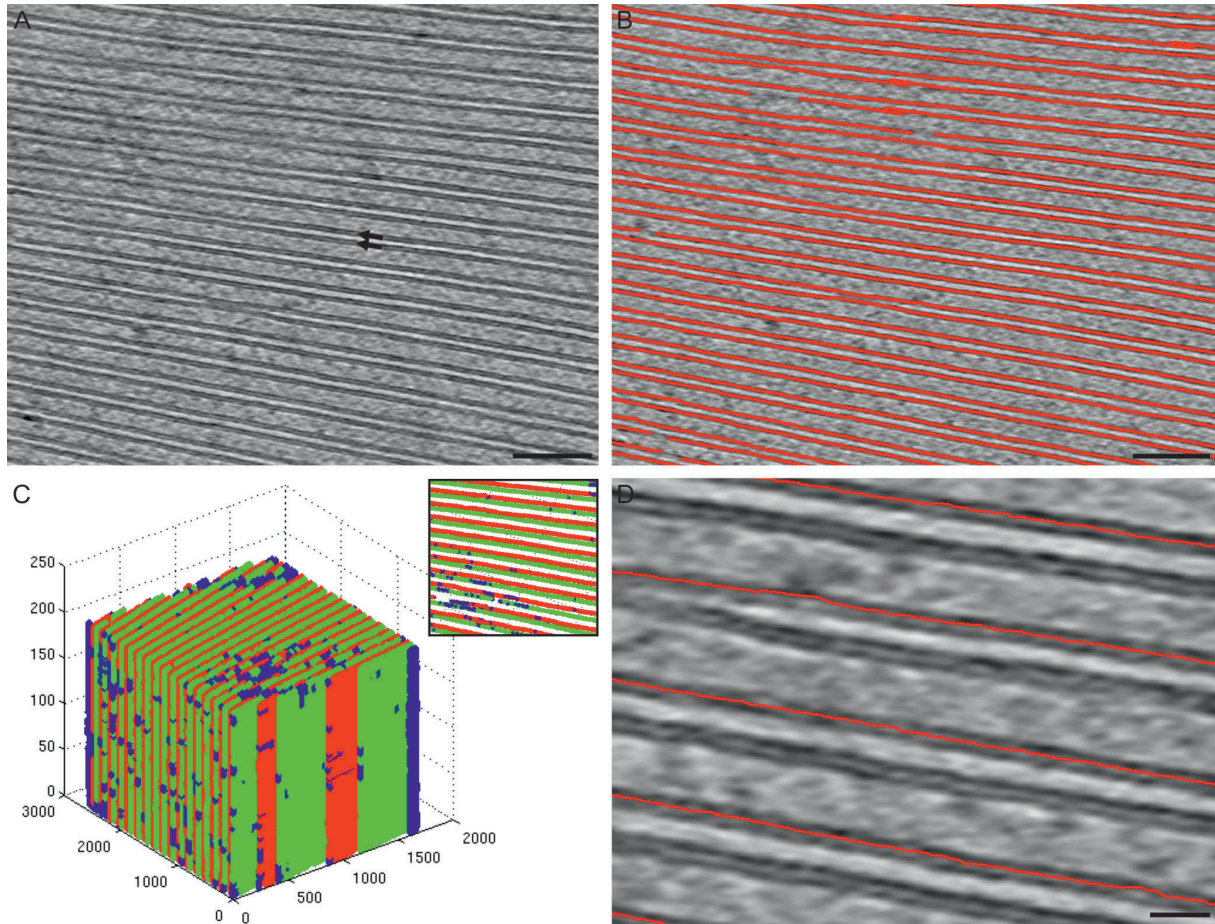


Figure S2, related to Figure 2 and 3. Segmentation of Disk Membranes

(A) Electron micrograph of a stack of disks. Black arrows indicate two membranes of one disk. (Scale bar 50 nm).

(B) The segmented disk membranes are shown in red. (Scale bar 50 nm).

(C) Three-dimensional representation of the segmented disk membranes. The segmented membranes were skeletonized using morphological operations. The skeletons of each disk are classified into two groups (labeled red and green) in order to take into account the extracellular and cytoplasmic sides of the rhodopsin molecules within the disk membranes.

Deformed regions of membranes were discarded (labeled in blue). One slice through the 3D segmented volume is shown in the inset.

(D) Skeletonization of one group of segmented membranes. The skeleton is used for subsequent particle (i.e. rhodopsin molecules) detection within the membrane bilayer (see also Figure S3-S4). (Scale bar 20 nm).

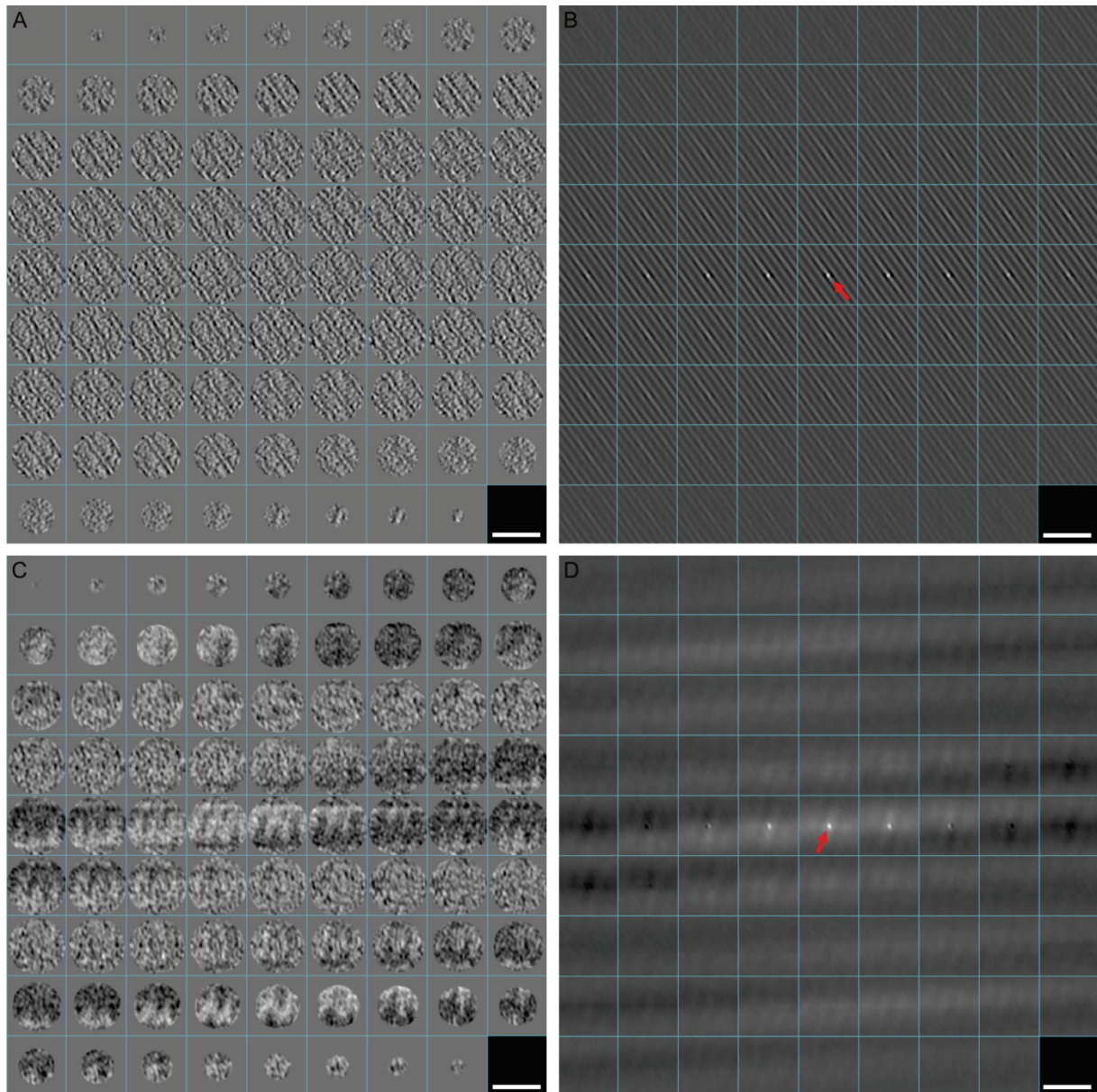


Figure S3, related to Figure 3. Angles determination for sub-tomogram averaging of disk membranes

(A) Gallery representation of an extracted particle sub-tomogram viewed from the side of the membrane. The sub-tomogram has been smoothed and two-times binned for clarity.

(B) Gallery representation of the autocorrelation function of the sub-tomogram in (A). The autocorrelation function was used to determine Psi (according to Euler's convention corresponds to in-plane rotation around Z-axis).

(C) Gallery representation of the enface view of the sub-tomogram shown in (A) after it correction for Psi.

(D) Gallery representation of the corresponding autocorrelation function of (C). The autocorrelation function was used to determine the second angle, Theta according to Euler's convention. Arrows indicate the main orientations of this particle at Psi and Theta. The third angle, Phi was scanned during the alignment procedure. (Scale bars 80 nm).

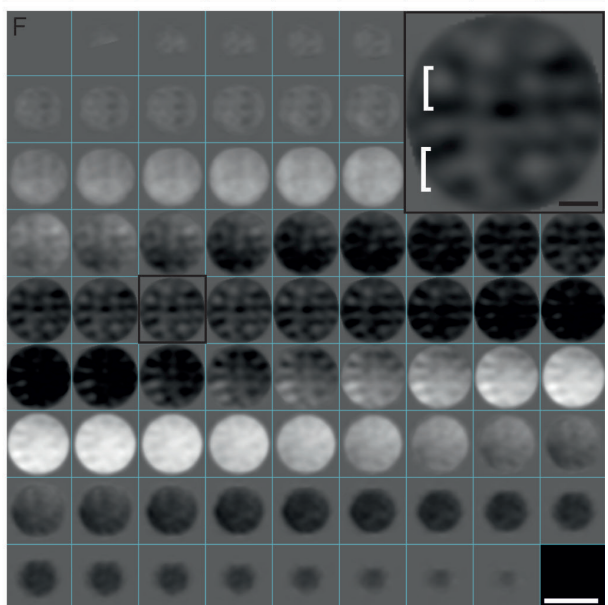
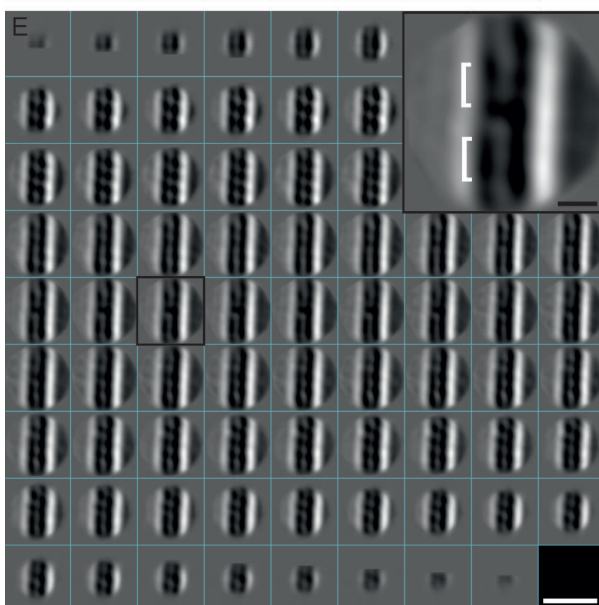
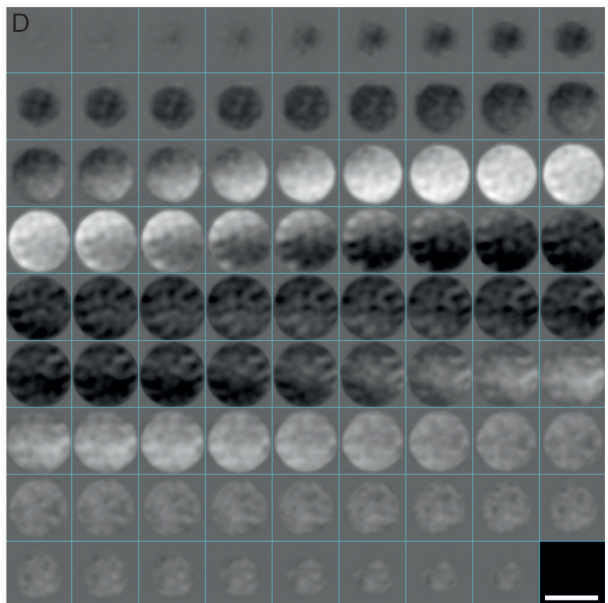
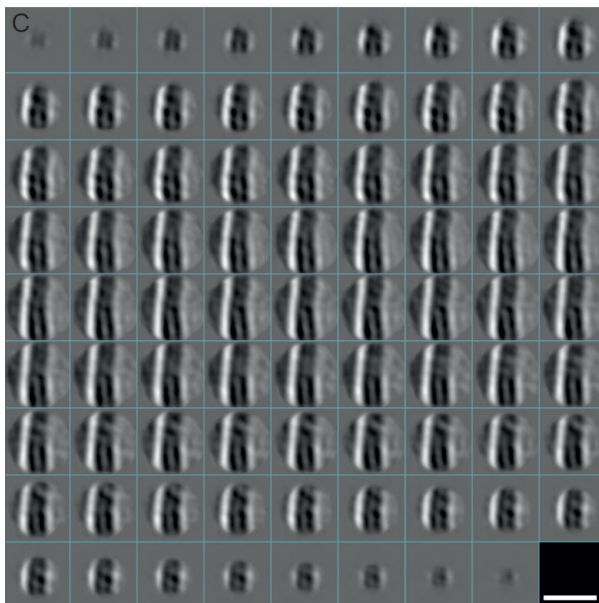
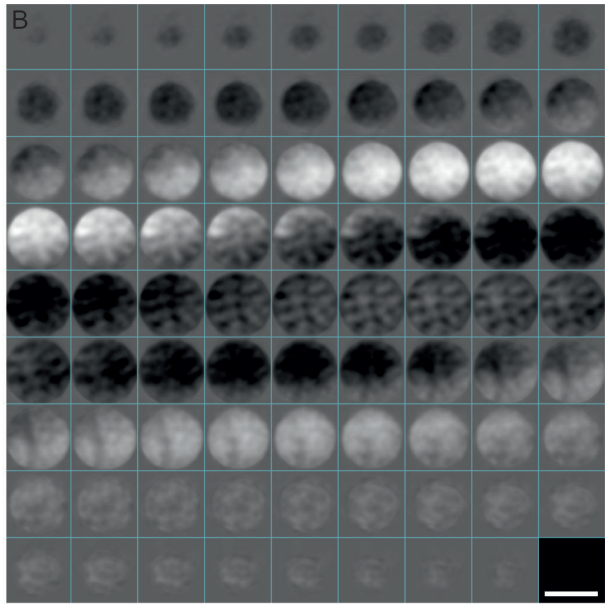
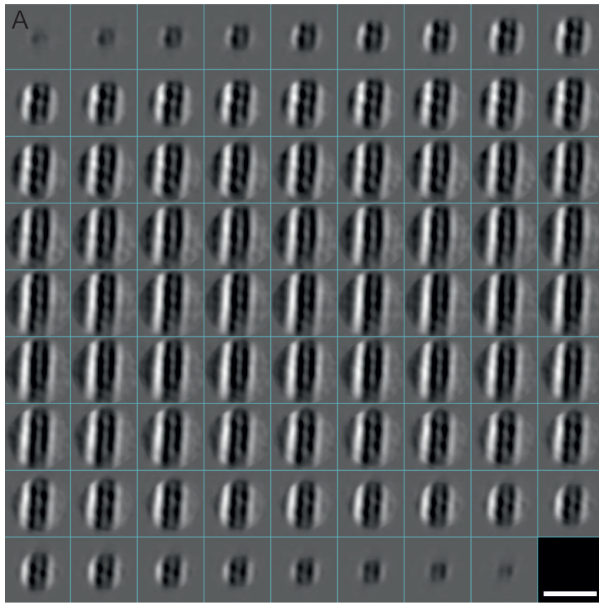


Figure S4, related to Figure 3 and 4. Classification of disk membranes and sub-tomogram averaging after refinement at full resolution

(A and B) Class average of sub-tomograms used for refinement. These sub-tomograms have intact membranes and show clear structure.

(C and D) Class average was discarded from averaging. Although some structure can be visualized, some sub-tomograms with deformed membranes made average poorer and thus they were discarded from subsequent averaging. (Scale bars 20 nm).

(E) Gallery of a sub-tomogram average of the disk membrane after refinement seen from the side. (Scale bar 20 nm). Inset, enlargement of the boxed area. Dimers of rhodopsin can be identified (white brackets). (Scale bar 5 nm).

(F) Gallery of the sub-tomogram average of the membrane after refinement seen from the top. Scale bar 20 nm. Inset, enlargement of the boxed area. Double rows of dimers can be visualized (white brackets). (Scale bar 5 nm).

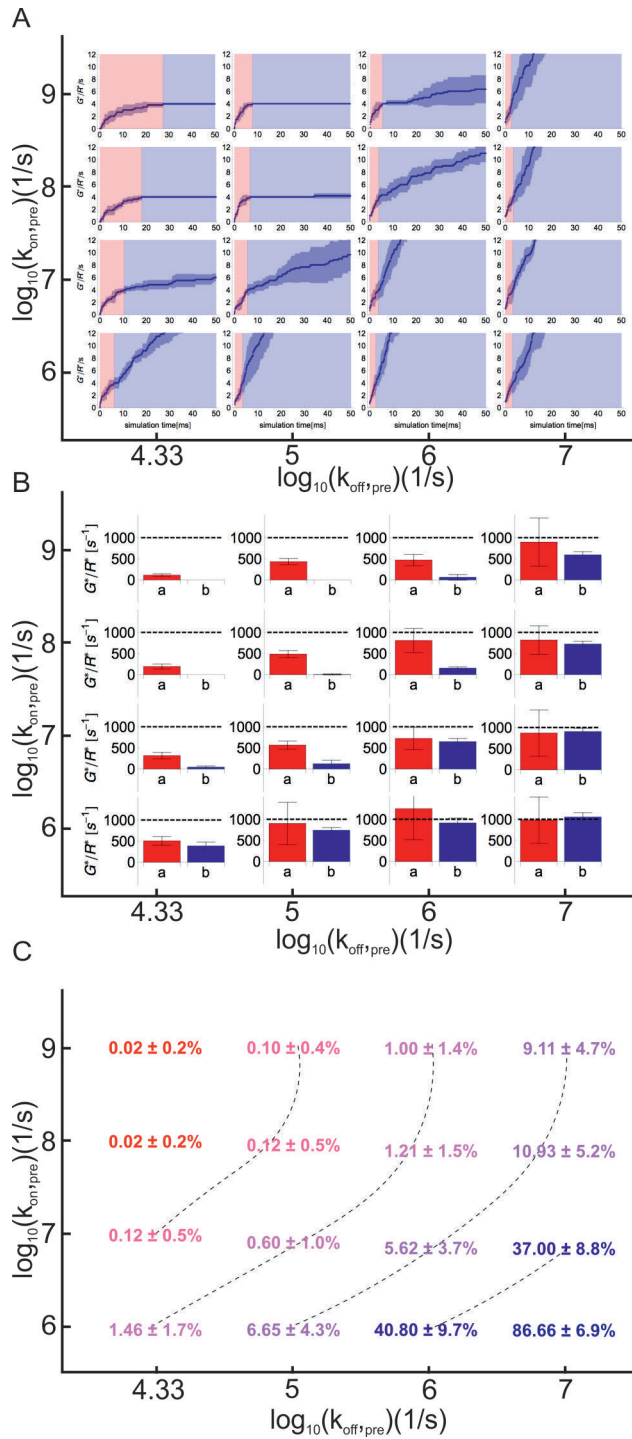


Figure S5, related to Figure 6. Parameter range showing biphasic kinetics

(A) The full kinetic scheme (Figure 6C, kinetic scheme) with $k_{\text{act}} = 1000 \text{ s}^{-1}$ is simulated with different *on*- and *off* rates for the pre-complex reaction. Two kinetic phases are compared in the simulation of a minimal track with 4 G_t molecules: phase (a), until all 4 G_t molecules have

been activated (red), and phase (b) after the 4 G_t molecules have been activated. The biphasic kinetics is observed for high *on* rates, and *off* rates smaller than 10^6 s^{-1} .

(B) Comparison of the G_t activation rates for the two phases (a) and (b) using the parameter combinations from (A). The biphasic kinetic behavior is manifested by high initial activation rates that are followed by very slow rates.

(C) The fraction of free *versus* total G_t is compared between the different parameter combinations from (A). Biphasic kinetics is closely related to low fractions of free G_t ; free G_t molecules participate in inter-track diffusion and thus equilibrate the system. Biphasic kinetics only occurs if the intra-track diffusion and activation of G_t is faster than the transit time of G_t between tracks.

Supplemental Video Legends

Video S1, related to Figure 3. 3D Reconstruction of a longitudinal section of a rod outer segment.

3D reconstruction (Figure 3) of a 50 nm-thick longitudinal section was generated using weighted back-projection algorithms in *etomo* (Mastronarde, 1997). The bilayer of the disk membranes are visible. Traverse densities crossing the bilayers corresponding to putative rhodopsin molecules as well as filament-like structures spanning the interdisk space can also be visualized.

Video S2, related to Figure 2. 3D Reconstruction of a cross section of a rod outer segment

3D reconstruction of a 50 nm-thick cross section (Figure 2) was generated using weighted back-projection algorithms in *etomo* (Mastronarde, 1997). This tiltseries was aligned using markless alignment in *etomo*. The reconstruction comprises three disks. The reconstruction was smoothed with a Gaussian filter and 2x binned in order to reduce the noise and enhance the contrast. Putative rows of rhodopsin occupying the entire disk surface can be seen running approximately along the incisure.

Video S3, related to Figure 3A. Animation of a 3D reconstruction of an oblique section

Animation of the 3D reconstruction of Figure 3A, visualized in the oblique view. Note the highly ordered electron-dense structures, corresponding to rows of dimers aligned parallel to the incisure. The ordered structure is observed on all disk membranes, suggesting long-range order of rhodopsin throughout the entire rod. Regions void of structure correspond to inter- or intra-disk space.

Video S4, related to Figure 3, 4B and 4C. Animation of a sub-tomogram average

Animation of the 3D sub-tomogram average, shown in Figure 3. Sub-tomograms were extracted around positions with low intensities along the bilayer of the disk membrane. The extracted sub-tomograms were translationally and rotationally aligned and averaged. The rhodopsin molecules appear here in dark (see also Figures 4B and 4C). The video walks through the 3D average, first bottom-top, in a plane parallel to the disk surface (top view) and then back-front through the disk membrane (side view). Isosurface representation appears in purple.

Video S5, related to Figure 5B and 6C. Animation of a reaction-diffusion simulation showing biphasic kinetics

Animation of the reaction-diffusion simulation with topology shown in Figure 5B (iii) and kinetic behavior shown in the red curve in Figure 6C for a total time of 50 ms. The first frame shows an already formed activation complex R^*G_t (violet) between the single R^* (yellow) and G_t (blue) and three other pre-complexed G_t s (green). G_t s rapidly associate with R to a pre-complex and dissociate again, forming a pre-complex with another R nearby, generating a hopping motion on tracks. All G_t s of the central track get activated over the first 5 ms. Afterwards the kinetics is dominated by the rare event that a G_t unbinds from R and does not rebind to the same track but dissociates and diffuses to another one. At around 37 ms such a rare event has happened and a R^*G_t complex is formed with a G_t that came from another track. G_t^* molecules are assumed to dissociate from the membrane and, therefore, are not visible.

References

- Mastrorade, D.N. (1997). Dual-axis tomography: an approach with alignment methods that preserve resolution. *J Struct Biol* 120, 343-352.
- Otsu, N. (1979). Threshold Selection Method from Gray-Level Histograms. *Ieee T Syst Man Cyb* 9, 62-66.